



Journal Name

ARTICLE

## One-step solid phase synthesis of highly efficient and robust cobalt pentlandite electrocatalyst for oxygen evolution reaction†

Mohammad Al-Mamun,<sup>a</sup> Yun Wang,<sup>\*a</sup> Porun Liu,<sup>a</sup> Yulin Zhong,<sup>a</sup> Huajie Yin,<sup>a</sup> Xintai Su,<sup>a,b</sup> Haimin Zhang,<sup>c</sup> Huagui Yang,<sup>a</sup> Dan Wang,<sup>a</sup> Zhiyong Tang,<sup>a</sup> Huijun Zhao<sup>\*ac</sup>

Received 00th January 20xx,  
Accepted 00th January 20xx

DOI: 10.1039/x0xx00000x

[www.rsc.org/](http://www.rsc.org/)

Cobalt pentlandite (Co<sub>9</sub>S<sub>8</sub>) has recently emerged as an alternative non-noble metal based electrocatalyst for the oxygen evolution reaction (OER). Co<sub>9</sub>S<sub>8</sub> is known for its intrinsic structural and electronic properties favorable for electrocatalytic applications, but the synthesis of stoichiometrically optimal Co<sub>9</sub>S<sub>8</sub> electrocatalysts remains challenging. Herein, a facile one-step solid phase calcination approach is presented in which Co<sub>9</sub>S<sub>8</sub> nanoparticles (NPs) were concurrently synthesised on carbon nanosheets (CNSs). The reaction mechanism for this synthesis was systematically investigated using TG/DSC-MS analysis. Relative to other cobalt chalcogenide electrocatalysts, the as-prepared thermally stable nanocomposite (Co<sub>9</sub>S<sub>8</sub>/CNS) has better electrocatalytic performance for OER in alkaline electrolyte, exhibiting a smaller overpotential of 294 mV at current density of 10 mA cm<sup>-2</sup> with a Tafel slope of 50.7 mV dec<sup>-1</sup>. Furthermore, a minimum overpotential of 267 mV with Tafel slope of 48.2 mV dec<sup>-1</sup> could be achieved using highly conducting multi-walled carbon nanotubes (MWCNT) as a conducting filler in the nanocomposites.

### Introduction

The oxygen evolution reaction (OER) is an important half reaction in electrochemical water splitting in sustainable and efficient energy conversion and storage technologies, such as water electrolyzers, solar water-splitting devices and rechargeable metal-air batteries.<sup>1-3</sup> However, the OER (4OH<sup>-</sup> → 2H<sub>2</sub>O + 4e<sup>-</sup> + O<sub>2</sub>) occurs through a thermodynamically unfavourable four-electron transfer process, which is kinetically sluggish<sup>4</sup> and involves a high overpotential to match the current density (~10 mA cm<sup>-2</sup>) required for solar fuel synthesis<sup>5</sup>. Currently, noble metal based oxides (e.g. RuO<sub>2</sub> and IrO<sub>2</sub>) are the benchmark OER catalysts<sup>6, 7</sup> but their elemental scarcity and prohibitive cost limit the widespread utilisation of such catalysts. Therefore, the development of efficient, earth-abundant and low cost OER catalysts is of paramount significance for future energy conversion and storage applications.<sup>8, 9</sup>

To date, a wide variety of OER electrocatalysts have been developed, such as transition-metal hydroxides,<sup>8</sup> oxides,<sup>10-13</sup> phosphides,<sup>14</sup> chalcogenides<sup>15-17</sup> and metal-free electrocatalysts<sup>18-21</sup>. Of these, cobalt sulfides (CoS,<sup>22</sup> CoS<sub>2</sub>,<sup>23</sup>

Co<sub>2</sub>S<sub>3</sub>,<sup>24</sup> Co<sub>3</sub>S<sub>4</sub>,<sup>25</sup> Co<sub>4</sub>S<sub>3</sub>,<sup>24</sup> and Co<sub>9</sub>S<sub>8</sub><sup>26, 27</sup>) are of particular interest due to their unique electronic structure,<sup>28, 29</sup> rich structural diversities, low cost and high electrocatalytic activities for OER<sup>30-32</sup>. Recent reports showed that the cobalt pentlandite (Co<sub>9</sub>S<sub>8</sub>) appears to be particularly promising for OER due to the large molecular cluster structure.<sup>30, 33, 34</sup>

In addition, theoretical studies also suggest the superior stability of Co<sub>9</sub>S<sub>8</sub> over other cobalt sulfides owing to its unique crystal structure.<sup>35</sup> In the primitive unit cell of Co<sub>9</sub>S<sub>8</sub>, there is one Co atom at the octahedral site (Co(O)), and the remaining eight Co atoms are at the tetrahedral sites (Co(T)). The formation of Co(O) and S further stabilises the Co<sub>9</sub>S<sub>8</sub> crystals. Co<sub>9</sub>S<sub>8</sub> possesses the optimal number of electrons per atom, which has a significant impact on its high heat of formation ( $\Delta H_f$ ). In comparison to the other transition metal sulfides with the same stoichiometry, Co<sub>9</sub>S<sub>8</sub> has the largest  $\Delta H_f$  value, further validating its superior stability. Moreover, the density of states (DOS) of Co<sub>9</sub>S<sub>8</sub> indicates pseudometallic characteristics and therefore, good electronic conductivity. Additionally, its Fermi energy level is located in the middle of the pseudogap, suggesting fully occupied and almost empty bonding and anti-bonding states, respectively. This molecular electronic configuration facilitates the required level of chemical interaction between the O atoms in the water molecule and the empty anti-bonding states in metal cations during the initial stage of the OER process. These theoretical modelling results suggest the structural-enhanced mechanism of Co<sub>9</sub>S<sub>8</sub> electrocatalyst for OER that reflect experimental observations.<sup>30, 33, 36-38</sup>

To realise the benefits mentioned above, precise control of the atomic stoichiometry in Co<sub>9</sub>S<sub>8</sub> synthesis is critically

<sup>a</sup> Centre for Clean Environment and Energy, Griffith University, Gold Coast Campus, QLD 4222, Australia. E-mail: [h.zhao@griffith.edu.au](mailto:h.zhao@griffith.edu.au); [yun.wang@griffith.edu.au](mailto:yun.wang@griffith.edu.au)  
Fax: +61 7 5552 8067; Tel: +61 1 5552 8261

<sup>b</sup> Ministry Key Laboratory of Oil and Gas Fine Chemicals, College of Chemistry and Chemical Engineering, Xinjiang University, Urumqi 830046, P.R. China.

<sup>c</sup> Centre for Environmental and Energy Nanomaterials, Institute of Solid State Physics, Chinese Academy of Sciences, Hefei 230031, P. R. China.

† Electronic Supplementary Information (ESI) available: [XRD, SEM, BET-BJH isotherms, EDS, FTIR, and Electrochemical characterisations]. See DOI:10.1039/x0xx00000x

important. However, the complex bonding modes between cobalt and sulfur make the desired stoichiometric  $\text{Co}_9\text{S}_8$  synthesis relatively challenging and often results in intricate crystal structure.<sup>39</sup> To date, a number of synthetic methods including hydrothermal,<sup>40</sup> solution-phase,<sup>41, 42</sup> and wet-chemical<sup>26</sup> have been demonstrated. Pyrolysis has been a popular and fairly successful method of preparing such materials, but has several drawbacks, such as the use of toxic and hazardous gases ( $\text{H}_2$ ,  $\text{H}_2\text{S}$ ).<sup>43-45</sup> In addition, some of the pyrolysis techniques involve two-step<sup>44, 45</sup> calcination and the pyrolysis reaction mechanisms were not well understood.

Another huge challenge in the synthesis of  $\text{Co}_9\text{S}_8$  is the aggregation of  $\text{Co}_9\text{S}_8$  nanoparticles (NPs),<sup>46, 47</sup> which not only decreases the effective active surface area but also introduces grain boundaries and defects<sup>48</sup> detrimental to electronic conductivity. Thus, nanostructuring of  $\text{Co}_9\text{S}_8$  onto a conductive carbonaceous support (graphene, carbon nanotubes (CNT) and carbon nanosheets (CNSs)) is a good approach for improved electronic conductivity and electrocatalytic active surface area. However, the uniform distribution and synergistic bonding between the NPs and predefined carbon nanostructures lead to a simple physical interface connection.<sup>30, 33, 34, 49-51</sup> As such, a novel one-step concurrent calcination approach warranting intimate connectivity of  $\text{Co}_9\text{S}_8$  NPs with the carbon nanostructures (CNS) is of fundamental interest to accelerate the development of  $\text{Co}_9\text{S}_8$  electrocatalysts for OERs, with an in-depth understanding of the pyrolysis mechanism.

Herein, a one-step concurrent growth of  $\text{Co}_9\text{S}_8$  NPs and carbon nanosheet ( $\text{Co}_9\text{S}_8/\text{CNS}$ ) composites from the pyrolytic transformation of cobalt-oleate ( $\text{Co}(\text{OA})_2$ ) to  $\text{Co}_9\text{S}_8/\text{CNS}$  nanocomposites in the presence of  $\text{Na}_2\text{SO}_4$  salt is reported. At moderately high temperature (700 °C), the  $\text{Co}(\text{OA})_2$  precursor can undergo concurrent sulfidation and carbonisation. The amorphous carbon reduces  $\text{SO}_4^{2-}$  ions to produce  $\text{S}^{2-}$  in the form of  $\text{H}_2\text{S}$  for the sulfidation of the Co precursor to yield  $\text{Co}_9\text{S}_8$  NPs and the resulting  $\text{Co}_9\text{S}_8/\text{CNS}$  nanocomposite. The nanocomposite exhibited superior electrocatalytic activity for OER in alkaline electrolyte and excellent stability compared to all other cobalt chalcogenides and most noble metal based electrocatalysts reported to date.

## Experimental section

### Preparation of $\text{Co}_9\text{S}_8/\text{CNS}$ nanocomposites

In a typical synthesis process, 1.0 mmol of  $\text{Co}(\text{NO}_3)_2 \cdot 6\text{H}_2\text{O}$  (Sigma-Aldrich, ACS reagent,  $\geq 98\%$ ) was dissolved in 20 mL of Milli-Q water (18  $\Omega$ ), then 2 mmol sodium oleate (NaOA) (TCI Co.) was added to the mixture, followed by 30 mL n-hexane (Sigma-Aldrich, HPLC grade,  $\geq 95\%$ ) and 20 mL ethanol (Chem-Supply). The resulting suspension was refluxed at 70 °C for 1 h with continuous stirring leading to the formation of cobalt oleate ( $\text{Co}(\text{OA})_2$ ). Thereafter, the suspension was cooled to room temperature and poured into a separatory funnel. The bottom aqueous layer containing unreacted metal species and oleate (OA) was drained off and the purple top organic layer

containing  $\text{Co}(\text{OA})_2$  was collected. 15.0 g of anhydrous  $\text{Na}_2\text{SO}_4$  (AR grade, Univar) was added to the above suspension and dried at 80 °C in an oven. This solid mixture was ground, and during this process,  $\text{Co}(\text{OA})_2$  was uniformly coated on the surface of  $\text{Na}_2\text{SO}_4$  particles. This ground powder was calcinated at 500 to 900 °C at a heating rate of 10 °C  $\text{min}^{-1}$  under continuous Ar flow (20 sccm) and held for 3 h in a tubular furnace. After cooling under Ar, the product was washed with copious amounts of water and recovered *via* centrifugation at 12000 rpm at least five times. After that, absolute ethanol was used for the final wash and the black powder was dried at 60 °C for 24 h in air and denoted as  $\text{Co}_9\text{S}_8/\text{CNS}$ . Pure  $\text{Co}_9\text{S}_8$  was also synthesised according to the literature reported elsewhere<sup>50</sup> and calcined at 700 °C under Ar atmosphere.

### Preparation of $\text{Co}_9\text{S}_8/\text{CNS}/\text{CNT}$ nanocomposites

Commercial (Shenzhen NTP Company, China) multi-walled carbon nanotubes (MWCNTs) with average range of diameter and length of 40-60 nm and 5-15  $\mu\text{m}$ , respectively, were partially oxidised by a modified Hummers method<sup>8</sup> and dispersed in Milli-Q water to form a 5 mg  $\text{mL}^{-1}$  dispersion. Subsequently, 1.0 mmol of  $\text{Co}(\text{NO}_3)_2 \cdot 6\text{H}_2\text{O}$  was dissolved in a given volume of CNT dispersion, followed by the same procedure described above to prepare the final nanocomposites. Five nanocomposites containing different amounts of CNTs were prepared and denoted as  $\text{Co}_9\text{S}_8/\text{CNS}/\text{CNT}-1$  (16.0 wt% CNT content),  $\text{Co}_9\text{S}_8/\text{CNS}/\text{CNT}-2$  (25.3% CNT),  $\text{Co}_9\text{S}_8/\text{CNS}/\text{CNT}-3$  (34.8% CNT),  $\text{Co}_9\text{S}_8/\text{CNS}/\text{CNT}-4$  (42.0% CNT) and  $\text{Co}_9\text{S}_8/\text{CNS}/\text{CNT}-5$  (47.3% CNT).

### Materials characterisation

The identification of bulk crystal phase and other relevant crystal structural information of the materials studied in this work were characterised by X-ray diffraction (XRD, Bruker D8 Advance diffractometer, equipped with a graphite monochromator) and Raman spectroscopic (Renishaw 100 system Raman spectrometer using 632.8 nm He-Ne laser) techniques. The surface morphology and nanostructural characterisations were conducted using a scanning electron microscope (SEM) equipped with an energy-dispersive X-ray spectrometer (EDS) (JSM-7100F) and a transmission electron microscope (TEM, Philips F20) linked with an EDS (Oxford) mapping device. The Brunauer-Emmett-Teller (BET) method was utilised to calculate the specific surface area (SBET) using nitrogen adsorption-desorption isotherms, while pore size distribution was calculated using the Barrett, Joyner and Halenda (BJH) method in Quantachrome Autosorb-1 equipment. The chemical compositions of the samples were analysed by X-ray photoelectron spectroscopy (XPS, Kratos Axis ULTRA with a 165 mm hemispherical electron energy analyser). The thermal processes of the precursors were characterised by heating the precursor from 100 to 900 °C with a ramp rate of 10 °C  $\text{min}^{-1}$  in an inert (Ar) atmosphere with TG/DSC (TG/DSC, Netzsch STA 449F3) and online gas MS spectrometer (MS, OmniStar GSD 320). The transmission

mode Fourier transform infrared spectroscopic (FTIR) analysis of the samples was carried out using a Perkin Elmer spectrum 1000 FTIR spectrometer with KBr as reference matrix. An inductively coupled plasma optical emission spectroscopy (ICP-OES, Agilent 710) was used to estimate the total Co content in the nanocomposite, where the limit of detection (LOD) for Co was  $0.3 \mu\text{g L}^{-1}$ .

### Electrochemical measurements

To evaluate the OER catalytic performance, a homogeneous ink was first prepared by adding 4.0 mg of catalyst in 1 mL of a solvent mixture of Nafion (5%), absolute ethanol and Milli-Q water with a volume ratio of 1:1:8, followed by sonication in an ultrasonic bath for at least 1 h.  $12.0 \mu\text{L}$  (loading of  $0.24 \text{ mg cm}^{-2}$ ) of the catalyst ink was drop casted on a clean rotating disk electrode (RDE) and dried in air at room temperature. The OER activities were measured in a standard three-electrode system, where the catalyst loaded RDE, an Hg/HgO (1.0 M NaOH) electrode and platinum mesh were the working, reference and counter electrode, respectively. The electrochemical responses were recorded using a potentiostat (CHI 760D, CH Instruments, USA) and the current density was normalised to the geometric area of the RDE ( $0.196 \text{ cm}^2$ ). The polarisation curves and Tafel plots were obtained at scan rates of 5 and  $1 \text{ mV s}^{-1}$ , respectively. All potentials in this work are reported with respect to the reversible hydrogen electrode (RHE) scale using the equation  $E_{\text{RHE}} = E_{\text{Hg/HgO}} + 0.059 \times \text{pH} + 0.098$ , where  $\text{pH} = 14$  in 1.0 M KOH electrolyte. The polarisation curves were corrected with 95%  $iR$ -compensation. For rotating ring disk electrode (RRDE) measurements, a RRDE with a glassy carbon disk (5 mm in diameter) and a Pt ring (Pine Instrument Co. Ltd. USA) were used. To ensure the anodic current originates from OER rather than other side reactions, the ring (Pt) potential was set at 0.4 V (vs. RHE) to reduce the  $\text{O}_2$  produced from the catalyst loaded on the disk electrode in  $\text{N}_2$ -saturated 1 M KOH solution. To monitor  $\text{HO}_2^-$  formation, the ring potential was held at 1.5 V (vs. RHE) for oxidising  $\text{HO}_2^-$  intermediates in  $\text{N}_2$ -saturated 1.0 M KOH electrolyte. The disk potentials for both measurements were set at 1.52 V (vs. RHE) with a rotating speed of 1600 rpm. AC impedance measurements were carried out under the same experimental configuration at overpotential of 270 mV at frequencies ranging from  $10^5$  to  $10^1$  Hz with the applied potential amplitude of 5 mV. Chronopotentiometric (CP) and chronoamperometric (CA) stability were tested at current density of  $10 \text{ mA cm}^{-2}$  and applied potential of 1.53 V (vs. RHE), respectively, for 10 h.

The TOF values were calculated from eqn (1):

$$\text{TOF} = \frac{J \times A}{4 \times F \times n} \quad (1)$$

where  $J$  ( $\text{A cm}^{-2}$ ) is the measured current density at  $\eta = 300$  mV;  $A$  ( $0.196 \text{ cm}^2$ ) is the area of RDE;  $F$  ( $96485.3 \text{ C mol}^{-1}$ ) is Faraday's constant; and  $n$  is the number of moles of the active material. TOF values were calculated assuming all metals were active during OER catalysis.

The mass activity ( $\text{A g}^{-1}$ ) values were calculated from the catalyst loading  $m$  ( $0.24 \text{ mg cm}^{-2}$ ) and the measured current density  $J$  ( $\text{mA cm}^{-2}$ ) at  $\eta = 300$  mV, utilising the following eqn (2):

$$\text{Mass Activity} = \frac{J}{m} \quad (2)$$

### Results and discussion

The solid phase synthesis of  $\text{Co}_9\text{S}_8/\text{CNS}$  nanocomposites through of the one-step concurrent growth process was carried out *via* the calcination of cobalt-oleate ( $\text{Co}(\text{OA})_2$ ) (see Experimental section for details) over  $\text{Na}_2\text{SO}_4$  salt under inert (Ar) atmosphere (Fig. 1).

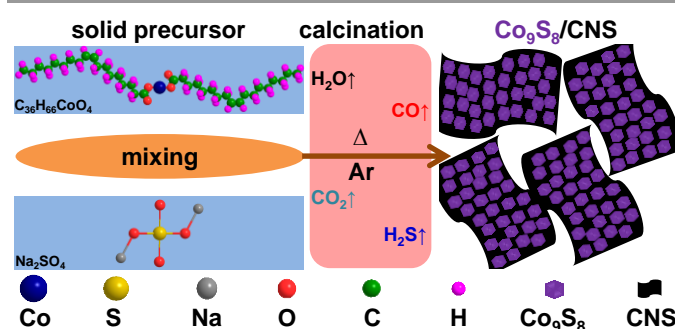
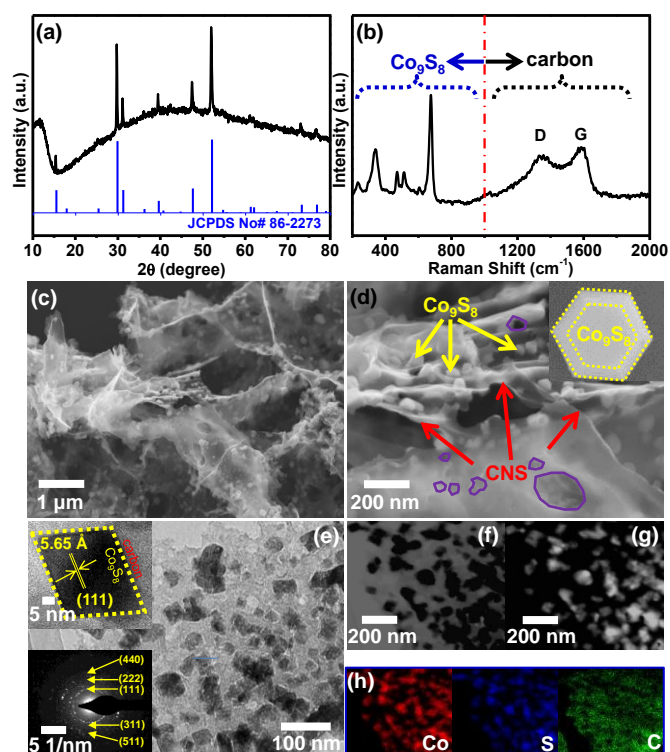


Fig. 1 Schematic illustration of the one-step concurrent growth approach showing that the emission of  $\text{H}_2\text{O}$ ,  $\text{CO}$ ,  $\text{CO}_2$  and  $\text{H}_2\text{S}$  gases during the calcination can promote the synthesis of  $\text{Co}_9\text{S}_8/\text{CNS}$  nanocomposite.

Fig. 2a shows the X-ray diffraction (XRD) pattern of the  $\text{Co}_9\text{S}_8/\text{CNS}$  nanocomposite prepared at  $700^\circ\text{C}$ , where the diffraction peaks can be indexed with the face centred cubic (fcc)  $\text{Co}_9\text{S}_8$  crystal structure (JCPDS 86-2273). In contrast, the XRD patterns (Fig. S1, ESI<sup>†</sup>) of the samples prepared below  $700^\circ\text{C}$  were mainly attributed to  $\text{CoO}$  and  $\text{Co}_3\text{O}_4$ . This suggests that an adequate level of thermal energy is necessary to facilitate the formation of pure  $\text{Co}_9\text{S}_8$  crystals. No diffraction peaks were observed for CNS or any other forms of cobalt sulfide. This implies that the pure  $\text{Co}_9\text{S}_8$  NPs were successfully synthesised and that the CNSs were not stacked in the graphitic form.<sup>52</sup> The Raman spectrum (Fig. 2b) of the  $\text{Co}_9\text{S}_8/\text{CNS}$  sample further confirms the formation of  $\text{Co}_9\text{S}_8$  NPs on CNSs with the characteristic Raman bands at 233.5, 341.7, 470.2, 511.1, 606.1 and  $675.8 \text{ cm}^{-1}$  for  $\text{Co}_9\text{S}_8$  along with the D and G bands at  $1341.2$  and  $1582.9 \text{ cm}^{-1}$  for the distorted graphitic carbon.<sup>50, 52, 53</sup>

The SEM images (Fig. 2c, Fig. S2 (ESI<sup>†</sup>)) of the  $\text{Co}_9\text{S}_8/\text{CNS}$  nanocomposite reveal the three-dimensional (3D) carbon nanostructures loaded with  $\text{Co}_9\text{S}_8$  NPs with negligible aggregations. The ultrathin mesoporous CNSs with the thickness of  $\sim 10$  nm were interconnected and the lateral size of each CNS was around several micrometres (Fig. S3, ESI<sup>†</sup>). As is evident from Fig. 2d, the hexagonal shaped  $\text{Co}_9\text{S}_8$  NPs with an average particle size of  $\sim 60$  nm were decorated on the CNS network. Higher calcination temperatures ( $>700^\circ\text{C}$ ) resulted in the formation of large aggregates (Fig. S4, ESI<sup>†</sup>), which are unfavourable for high catalytic performance in OERs. This result highlights that an optimum calcination temperature is

critical for preparing uniformly structured  $\text{Co}_9\text{S}_8/\text{CNS}$  nanocomposites. In addition, the BET analysis suggests that the specific surface area of  $\text{Co}_9\text{S}_8/\text{CNS}$  nanocomposite is  $80.27 \text{ m}^2 \text{ g}^{-1}$  (Fig. S5a, ESI<sup>†</sup>). Whereas, the pore size distribution curve in Fig. S5b (ESI<sup>†</sup>) confirms the mesoporous structure of the nanocomposite and is consistent with the pores indicated in Fig. 2d. The presence of abundant mesopores in the 3D CNS scaffold is beneficial for mass transport of reactants and products within the electrocatalysts and is advantageous for electrocatalytic OER applications.



**Fig. 2** (a) XRD pattern, (b) Raman spectrum, (c) low magnification SEM, (d) higher magnification SEM, (e) TEM, (f) bright-field, (g) dark-field TEM images and (h) Co, S and C distribution mapping of  $\text{Co}_9\text{S}_8/\text{CNS}$  nanocomposite. Inset in (d) shows hexagonal shaped  $\text{Co}_9\text{S}_8$  NP. The  $\text{Co}_9\text{S}_8$  NPs, CNSs and mesopores are indicated by yellow, red and purple arrow or lines, respectively. Insets in (e) show high resolution HRTEM (top left) and SAED pattern (bottom left).

Transmission electron microscopy (TEM) was used to further elucidate the crystal structure of  $\text{Co}_9\text{S}_8$  NPs. As shown in Fig. 2e, the  $\text{Co}_9\text{S}_8$  NPs can be clearly distinguished on the decorated CNSs. The selected area electron diffraction (SAED) pattern (bottom left in Fig. 2e) confirms the existence of the (111), (311), (222), (440) and (511) diffraction planes in the  $\text{Co}_9\text{S}_8/\text{CNS}$  nanocomposite, consistent with the XRD result (Fig. 2a). In addition, the high resolution TEM (HRTEM) image (top left in Fig. 2e) shows a lattice spacing of  $5.65 \text{ \AA}$ , corresponding to the (111) plane of the cubic fcc phase of  $\text{Co}_9\text{S}_8$  crystals.

Fig. 2f and 2g display the bright and dark-field scanning transmission electron microscopic (STEM) images of the  $\text{Co}_9\text{S}_8/\text{CNS}$  nanocomposite in which the NPs can be identified as black (Fig. 2f) and bright (Fig. 2g) spots, respectively. Furthermore, energy dispersive X-ray spectroscopy (EDS) mapping was carried out to map the elemental distribution

throughout the nanocomposite. As is evident from Fig. 2h, the NPs are composed of Co and S as evident from the overlapping elemental distribution of Co and S. The EDS mapping also indicates that the CNSs were not doped by sulfur. Additionally, low magnification EDS mapping (Fig. S6, ESI<sup>†</sup>) shows the uniform distribution of  $\text{Co}_9\text{S}_8$  NPs throughout the entire nanocomposite.

The X-ray photoelectron spectroscopy (XPS) survey spectrum (Fig. 3a) reveals the presence of Co, S, O and C elements in the nanocomposite. Fig. 3b shows the high resolution deconvoluted Co 2p spectrum, which displays two sets of doublets and shakeup satellites (abbreviated as "Sat."). The first doublet (at 779.5 and 795.4 eV) and the second (at 781.0 and 796.7 eV) can be assigned to Co  $2p_{3/2}$  and Co  $2p_{1/2}$ , respectively, consistent with the literature on the formation of  $\text{Co}_9\text{S}_8$ .<sup>26, 30, 37</sup> For the S 2p spectrum (Fig. 3c), two characteristic peaks centred at 161.6 and 162.8 eV correspond to S  $2p_{3/2}$  and S  $2p_{1/2}$  states attributed to the  $\text{S}^{2-}$  species bonded with Co atoms.<sup>26, 33</sup> In addition to  $\text{S}^{2-}$  states, the peak located at 168.5 eV associated with  $\text{S}^{6+}$  states might have resulted from the oxidised sulfur species on the  $\text{Co}_9\text{S}_8$  NPs' surface.<sup>54</sup> The C 1s spectrum (Fig. 3d) reveals that in addition to the main CNS carbon, C-C/C=C (at 284.6 eV), oxygen containing carbon species such as C-O (at 285.9 eV), C=O (at 286.7 eV) and O-C=O (at 288.7 eV) were present in the nanocomposite. These functional groups may be responsible for the uniformly distributed growth of  $\text{Co}_9\text{S}_8$  NPs. The FTIR spectrum (Fig. S7, ESI<sup>†</sup>) of the  $\text{Co}_9\text{S}_8/\text{CNS}$  sample shows two peaks at the frequencies of 1100 and  $620 \text{ cm}^{-1}$  related to the S-O bond and the lattice vibration of metal cations, respectively.<sup>55, 56</sup> The combination of XPS and FTIR analysis suggests that  $\text{Co}_9\text{S}_8$  NPs were bonded on the CNSs through interfacial S-O groups.<sup>57</sup>

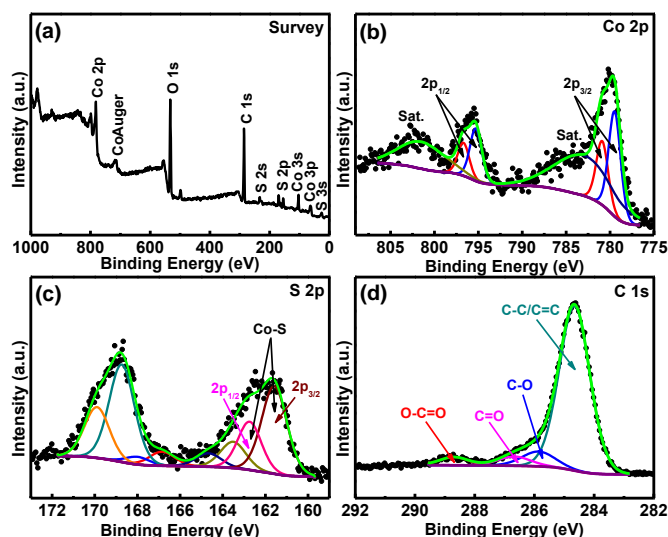


**Fig. 3** (a) XPS survey spectrum, and high resolution (b) Co 2p, (c) S 2p and (d) C 1s spectra of the  $\text{Co}_9\text{S}_8/\text{CNS}$  nanocomposite.

Inductively coupled plasma optical emission spectroscopy (ICP-OES) and thermogravimetric analysis (TGA) were used to determine the bulk composition of the  $\text{Co}_9\text{S}_8/\text{CNS}$  nanocomposite. The ICP-OES result confirmed the mass ratio of  $\text{Co}_9\text{S}_8$  (total cobalt) in  $\text{Co}_9\text{S}_8/\text{CNS}$  nanocomposite was 48.4%



by weight. On the other hand, TGA not only enables us to estimate the weight percentage of  $\text{Co}_9\text{S}_8$  but also to assess the thermal stability of the nanocomposite in air. The resultant TGA curve (Fig. 4a) suggested an initial weight loss of (~11.6%) within the temperature range of 50 to 400 °C which corresponds with the evaporation of adsorbed  $\text{H}_2\text{O}$  and decomposition of labile oxygen functional groups in the CNSs,<sup>58</sup> as detected by the XPS measurement. A further weight loss of ~14.9% is due to the oxidation of CNSs up to 500 °C. At ~500 °C, an obvious weight gain was observed due to the partial oxidation of  $\text{Co}_9\text{S}_8$  nanocrystals<sup>50</sup> to form  $\text{CoSO}_4$  (I). However, the TGA curve was almost stable at temperatures >800 °C due to the thermally oxidised  $\text{Co}_3\text{O}_4$  (II) from  $\text{Co}_9\text{S}_8$ , as confirmed by the XRD pattern (Fig. 4b). Based on the solid residue remaining as  $\text{Co}_3\text{O}_4$ , the amount of  $\text{Co}_9\text{S}_8$  was calculated to be 48.5% in the  $\text{Co}_9\text{S}_8/\text{CNS}$  nanocomposite, which is in good agreement with the ICP-OES result (48.4%).

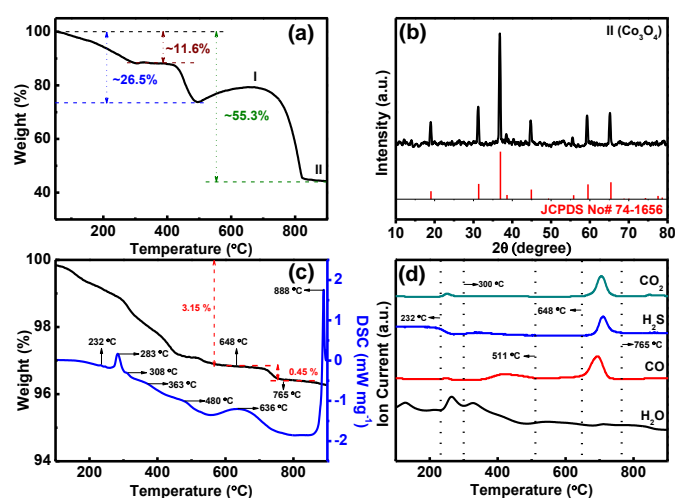


**Fig. 4** (a) TGA curve for  $\text{Co}_9\text{S}_8/\text{CNS}$  sample in air from 50 to 900 °C, (b) XRD pattern of the sample after burning the  $\text{Co}_9\text{S}_8/\text{CNS}$  nanocomposite at 900 °C in air, (c) TG/DSC and (d) MS curves of the precursor ( $\text{Co}(\text{OA})_2 + \text{Na}_2\text{SO}_4$ ) under Ar protection from 100 to 900 °C.

To understand the reaction mechanism for the concurrent growth of  $\text{Co}_9\text{S}_8/\text{CNS}$  nanocomposites, synchronous TG/DSC-MS data were collected and presented in Fig. 4c and 4d. According to our previous work,<sup>59</sup> the concurrently grown product is largely reliant on the corresponding decomposition characteristics of each component in the solid reaction precursor. Therefore, a certain amount of thermal energy is essential to trigger each decomposition product during the calcination. In Fig. 4c, the initial major breakdown started at 283 °C and continued up to 511 °C, as indicated by the endothermic DSC peak and simultaneous MS peaked emissions (Fig. 4d) of the gaseous products ( $\text{H}_2\text{O}$ ,  $\text{CO}$ , and  $\text{CO}_2$ ). This implies the decomposition of  $\text{Co}(\text{OA})_2$  to form  $\text{CoO}_x$  (Fig. S1, ESI<sup>†</sup>) and amorphous carbon (eqn (3)). A broad endothermic DSC peak from 550 to 765 °C with a sharp weight loss of 0.45% is related to the reduction of  $\text{Na}_2\text{SO}_4$  (eqn (4)) by carbon to produce  $\text{Na}_2\text{S}$ . Thereafter, the hydrolysis of  $\text{Na}_2\text{S}$  (eqn (5)) led to the formation of  $\text{H}_2\text{S}$ , which can transform the  $\text{CoO}_x$  to  $\text{Co}_9\text{S}_8$  nanocrystals (eqn (6)). The major gaseous

products were emitted between 648 to 765 °C, which suggests the concurrent carbonisation and sulfidation of the reaction precursor ( $\text{Co}(\text{OA})_2 + \text{Na}_2\text{SO}_4$ ). Also, the pyrolysis temperature of ~700 °C can be treated as the optimum condition to prepare uniformly structured  $\text{Co}_9\text{S}_8/\text{CNS}$  nanocomposite. Furthermore, a fraction of amorphous carbon produced during the initial heating process and the salt ( $\text{Na}_2\text{SO}_4$ ) were utilised to arrange the final  $\text{Co}_9\text{S}_8/\text{CNS}$  nanocomposite. This means that the solid salt ( $\text{Na}_2\text{SO}_4$ ) not only helps to grow the nanostructures on its surface but also supplies the adequate amount of sulfur species required for the one-step sulfidation process.

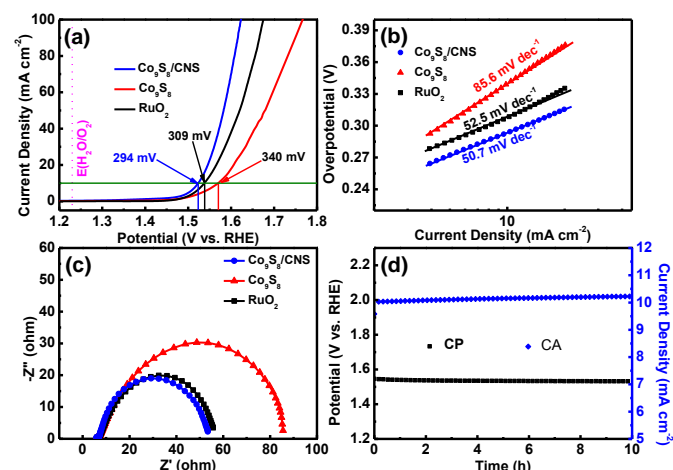
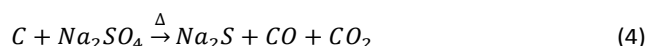
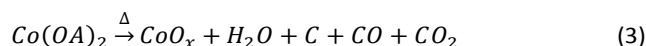


**Fig. 5** (a) Polarisation curves, (b) Tafel plots, (c) Nyquist plots of  $\text{Co}_9\text{S}_8/\text{CNS}$ ,  $\text{Co}_9\text{S}_8$  and  $\text{RuO}_2$  electrocatalysts; (d) CP and CA plots of the  $\text{Co}_9\text{S}_8/\text{CNS}$  catalyst in 1.0 M KOH electrolyte.

In this work, the electrocatalytic OER performances of  $\text{Co}_9\text{S}_8/\text{CNS}$  and other control samples, including  $\text{Co}_9\text{S}_8$  (Fig. S8, ESI<sup>†</sup>), and benchmark  $\text{RuO}_2$ , were evaluated in 1.0 M KOH electrolyte using a standard three-electrode system as described in the experimental section. Fig. 5a shows the polarisation curves of  $\text{Co}_9\text{S}_8/\text{CNS}$ ,  $\text{Co}_9\text{S}_8$  and commercial  $\text{RuO}_2$  electrocatalysts obtained at a scan rate of  $5 \text{ mV s}^{-1}$ . An obvious rise of the anodic current at an onset potential of ~1.45 V (vs. RHE) was observed for the  $\text{Co}_9\text{S}_8/\text{CNS}$  catalyst. This was ~20 mV earlier than that of pure  $\text{Co}_9\text{S}_8$  and  $\text{RuO}_2$ , indicating the superior intrinsic catalytic activity of the  $\text{Co}_9\text{S}_8/\text{CNS}$  catalyst towards OER. In addition, the overpotential required to reach the current density of  $10 \text{ mA cm}^{-2}$  was 294 mV for the  $\text{Co}_9\text{S}_8/\text{CNS}$  catalyst, 15 mV lower than that of  $\text{RuO}_2$  (309 mV) and significantly lower than that of  $\text{Co}_9\text{S}_8$  (340 mV), which demonstrates the importance of CNSs in improving the OER performance of the catalyst. Furthermore, the  $\text{Co}_9\text{S}_8/\text{CNS}$  nanocomposite exhibits the lowest OER overpotential at 10

$\text{mA cm}^{-2}$  in both 0.1 M and 1.0 M KOH electrolyte compared with any other cobalt chalcogenide-based electrocatalysts reported to date (see Table S1, S2, ESI<sup>†</sup>).

To assess the influence of overpotential on the steady-state current density, Tafel plots were constructed (Fig. 5b). The resulting Tafel slope of the  $\text{Co}_9\text{S}_8/\text{CNS}$  catalyst was  $50.7 \text{ mV dec}^{-1}$ , which was much lower than that of  $\text{Co}_9\text{S}_8$  ( $85.6 \text{ mV dec}^{-1}$ ) and slightly lower than  $\text{RuO}_2$  ( $52.5 \text{ mV dec}^{-1}$ ), demonstrating its superior OER kinetics. To understand the faster OER kinetics of the  $\text{Co}_9\text{S}_8/\text{CNS}$  sample, electrochemical impedance spectroscopy (EIS) technique was also employed to examine the charge transfer process in the catalysts (Fig. 5c). The charge transfer resistance ( $R_{ct}$ ) of  $\text{Co}_9\text{S}_8/\text{CNS}$  ( $46.8 \Omega$ ) was much smaller than that of  $\text{Co}_9\text{S}_8$  ( $79.1 \Omega$ ) and slightly lower than that of  $\text{RuO}_2$  ( $49.5 \Omega$ ), consistent with the Tafel measurements (Fig. 5b). The lowest  $R_{ct}$  value of the  $\text{Co}_9\text{S}_8/\text{CNS}$  catalyst demonstrates the importance of intimate connectivity between  $\text{Co}_9\text{S}_8$  NPs and CNSs within the nanocomposite, facilitating faster charge transfer during OER catalysis. In addition, the extent of electrocatalytic active sites was compared with the electrochemical double-layer capacitance ( $C_{dl}$ ).<sup>60</sup> The resulting  $C_{dl}$  value for the  $\text{Co}_9\text{S}_8/\text{CNS}$  catalyst was  $37.7 \text{ mF cm}^{-2}$ , whereas the  $C_{dl}$  values of  $\text{Co}_9\text{S}_8$  and  $\text{RuO}_2$  were 6.5 and  $9.9 \text{ mF cm}^{-2}$ , respectively (Fig. S9, ESI<sup>†</sup>). This significant difference in  $C_{dl}$  values between the  $\text{Co}_9\text{S}_8$  and  $\text{Co}_9\text{S}_8/\text{CNS}$  samples was a result of the largely aggregated micro-sized ( $\sim 1 \mu\text{m}$ )  $\text{Co}_9\text{S}_8$  NPs (Fig. S7b, ESI<sup>†</sup>) prepared in absence of any carbon support. The  $\text{Co}_9\text{S}_8$  NPs' size, on the other hand, was easily controlled on the scale of several tens of nanometres (Fig. 2d), further confirming the utility of the one-step concurrent growth method. Consequently, the  $\text{Co}_9\text{S}_8/\text{CNS}$  catalyst can offer larger amounts of electrocatalytic active sites compare to  $\text{Co}_9\text{S}_8$ , thereby supporting the superior OER catalytic performance.

In addition to its high electrocatalytic activity, the catalyst's stability is critical for energy conversion applications. The  $\text{Co}_9\text{S}_8/\text{CNS}$  catalyst's chronopotentiometry (CP) and chronoamperometry (CA) test results in 1.0 M KOH electrolyte are presented in Fig. 5d. The potential remained unchanged ( $\sim 1.53 \text{ V}$ ) at the current density of  $10 \text{ mA cm}^{-2}$  in the CP test, while the current density stayed close to  $\sim 10 \text{ mA cm}^{-2}$  at 1.53 V for the 10 h testing period. This shows the impressive electrocatalytic and cyclic (Fig. S10, ESI<sup>†</sup>) stability of the catalyst in alkaline media which matches the theoretical predictions.<sup>35</sup> The turnover frequency (TOF) and mass activity of  $\text{Co}_9\text{S}_8/\text{CNS}$  were  $0.1063 \text{ s}^{-1}$  and  $52.1 \text{ A g}^{-1}$ , respectively, which are much higher than those of  $\text{Co}_9\text{S}_8$  and  $\text{RuO}_2$  (see Table 1). It should be noted that the calculated TOF values represent the lower limit of the catalyst since not all active sites are electrochemically accessible during catalysis. More importantly, the TOF for the  $\text{Co}_9\text{S}_8/\text{CNS}$  catalyst was much higher than that of the previously reported metal sulfide catalysts.<sup>33</sup>

To ensure that the observed current originated from the OER process, a rotating ring-disk electrode (RRDE) was employed with a ring (Pt) potential of 0.40 V (vs. RHE) to reduce the generated  $\text{O}_2$  from the glassy carbon electrode

(GCE) disk. The simultaneous OER at the GCE disk and oxygen reduction reaction (ORR) at the Pt ring may detect the molecular  $\text{O}_2$ .<sup>61, 62</sup> As evident from Fig. S11a (ESI<sup>†</sup>), a constant disk current of  $619 \mu\text{A}$  (black line) resulting from molecular  $\text{O}_2$  generation on the  $\text{Co}_9\text{S}_8/\text{CNS}$  catalyst surface at the disk electrode was observed. The generated molecular  $\text{O}_2$  sweeps across the surrounding Pt ring electrode and are readily reduced. As a consequence, a ring current of  $\sim 121 \mu\text{A}$  (collection efficiency of 0.2) was recorded (blue line), confirming that the observed OER current catalysed by the  $\text{Co}_9\text{S}_8/\text{CNS}$  nanocomposite primarily originates from the desirable OER process with a Faradaic efficiency of 95–97% (Inset in Fig. S11a, ESI<sup>†</sup>). We also checked for the possible formation of hydrogen peroxide ( $\text{HO}_2^-$ ) intermediates by setting an applied potential of 1.5 V (vs. RHE) and oxidising these intermediates. As shown in Fig. S11b (ESI<sup>†</sup>), a lower level of the ring current ( $\approx 3.4 \mu\text{A}$ ) was detected (blue line) compared to the large disk current (black line), which confirmed a negligible amount of hydrogen peroxide produced during the OER catalysis. This provides a reasonable validation that the OER catalysed by  $\text{Co}_9\text{S}_8/\text{CNS}$  proceeded *via* a desired four-electron pathway.

Table 1 Comparison of OER electrocatalytic activity of various electrocatalysts in 1.0 M KOH electrolyte.

Catalysts	Onset potential (V)	$\eta@10 \text{ mA cm}^{-2}$ (mV) <sup>a</sup>	Tafel slope (mV $\text{dec}^{-1}$ )	$R_{ct}$ ( $\Omega$ )	Mass activity ( $\text{A g}^{-1}$ ) <sup>b,c</sup>	TOF ( $\text{s}^{-1}$ ) <sup>b,c,d</sup>
$\text{Co}_9\text{S}_8$	$\sim 1.47$	340	85.6	79.1	19.2	0.0808
$\text{Co}_9\text{S}_8/\text{CNS}$	$\sim 1.45$	294	50.7	46.8	52.1	0.1063
$\text{Co}_9\text{S}_8/\text{CNS}/\text{CNT1}$	$\sim 1.45$	275	50.3	45.1	84.3	0.4169
$\text{Co}_9\text{S}_8/\text{CNS}/\text{CNT2}$	$\sim 1.45$	267	48.2	41.7	117.2	0.6352
$\text{Co}_9\text{S}_8/\text{CNS}/\text{CNT3}$	$\sim 1.45$	295	52.2	57.1	48.8	0.3199
$\text{Co}_9\text{S}_8/\text{CNS}/\text{CNT4}$	$\sim 1.46$	299	59.2	71.7	42.0	0.3080
$\text{Co}_9\text{S}_8/\text{CNS}/\text{CNT5}$	$\sim 1.46$	305	84.1	102.4	32.7	0.2707
$\text{RuO}_2$	$\sim 1.47$	309	52.5	49.5	33.6	0.0116

<sup>a</sup>The values are calculated at their corresponding overpotential@10  $\text{mA cm}^{-2}$ ;

<sup>b</sup>The amount of  $\text{Co}_9\text{S}_8$  is only considered as active OER catalysts; <sup>c</sup>All calculations are done at an overpotential of 300 mV; <sup>d</sup>The values are calculated by presuming that all metal atoms are involved in the catalysis.

The  $\text{Co}_9\text{S}_8/\text{CNS}$  catalyst showed better performance than previously reported cobalt chalcogenide catalysts (see Table S1, S2, ESI<sup>†</sup>) in terms of electrocatalytic activity, kinetics, and stability. However, the overpotential required to achieve the current density of  $10 \text{ mA cm}^{-2}$  has a significant delay of  $\sim 74 \text{ mV}$  (Fig. 5a) with respect to its onset overpotential. We speculate that the electronic conductivity of CNSs which support the active material ( $\text{Co}_9\text{S}_8$ ) is not high enough to make the polarisation curve steeper. Based on this assumption, highly conductive multi-walled carbon nanotubes (MWCNT, denoted as "CNT") were added as conductive filler in the  $\text{Co}_9\text{S}_8/\text{CNS}$  nanocomposite. Different amounts of partially oxidised (see Experimental section for details) CNTs were added in the precursor before carrying out the one-step

calcination to ensure good dispersion of the CNTs throughout the nanocomposites.

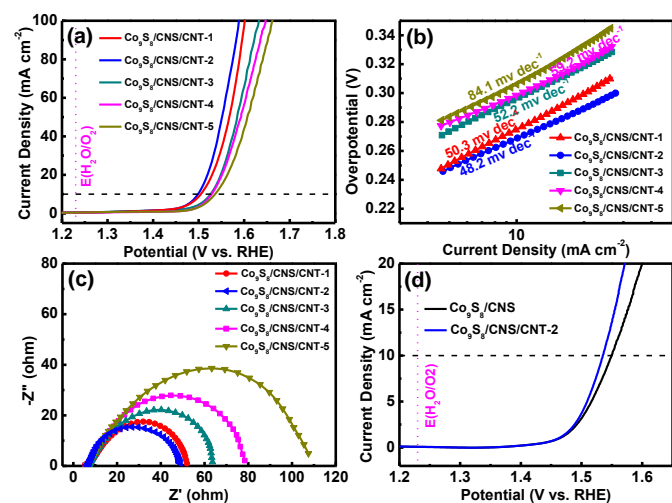


**Fig. 6** (a) Polarisation curves, (b) Tafel plots and (c) Nyquist plots of  $\text{Co}_9\text{S}_8/\text{CNS}/\text{CNT}$  nanocomposites with different percentages of CNTs in 1.0 M KOH; (d) polarisation curves for  $\text{Co}_9\text{S}_8/\text{CNS}$  and  $\text{Co}_9\text{S}_8/\text{CNS}/\text{CNT-2}$  electrodes in 0.1 M KOH electrolyte. The numerical suffix (1-5) in each composite name refers to the CNT weight percentage of 16.0, 25.3, 34.8, 42.0, and 47.3 %, respectively.

These  $\text{Co}_9\text{S}_8/\text{CNS}/\text{CNT}$  nanocomposites (Fig. S12, S13, ES1†) were applied as OER electrocatalysts in 1.0 M KOH electrolyte and their electrocatalytic OER activities (Fig. 6a) were highly dependent on the final composition of the catalysts (see Table S3, ES1†). As shown in Fig. 6a, the overpotential at  $10 \text{ mA cm}^{-2}$  decreased with the increase of CNT content from 16.0 to 25.3%. Further increase in CNT content resulted in inferior OER activity with higher overpotential. A minimum overpotential of 267 mV was achieved with the optimum 25.3% CNT in the nanocomposite. The  $\text{Co}_9\text{S}_8/\text{CNS}/\text{CNT-2}$  (25.3% CNT) electrode displayed the lowest Tafel slope of  $48.2 \text{ mV dec}^{-1}$  (Fig. 6b) among all the nanocomposites studied in this work. The low Tafel slope of the  $\text{Co}_9\text{S}_8/\text{CNS}/\text{CNT-2}$  electrode reflects its superior OER kinetics, which is consistent with its lowest  $R_{ct}$  value ( $41.7 \Omega$ ) (Fig. 6c). The poor performances associated with the samples containing a larger amount of CNTs (>25.3%) might be related to the reduced amount of active material ( $\text{Co}_9\text{S}_8$ ). The OER performance of both  $\text{Co}_9\text{S}_8/\text{CNS}$  and  $\text{Co}_9\text{S}_8/\text{CNS}/\text{CNT-2}$  catalysts were also tested in 0.1 M KOH electrolyte (Fig. 6d). By comparing the corresponding electrochemical OER parameters (see Table S1, Table S2, ES1†), it can be concluded that the synthesised catalysts perform better than any other cobalt-based chalcogenides reported to date.

## Conclusions

In summary, a novel concurrent growth approach has been demonstrated for the solid phase synthesis of a  $\text{Co}_9\text{S}_8/\text{CNS}$  nanocomposite and its application as an efficient electrocatalyst for oxygen evolution reaction (OER). This inexpensive, facile, one-step, and easily controllable synthetic method can enhance physico-chemical connectivity between

the nanoparticulate active materials ( $\text{Co}_9\text{S}_8$ ) and the carbon nanosheets (CNSs). More importantly, based on the TG/DSC-MS analysis, a plausible pyrolysis reaction mechanism for the preparation of  $\text{Co}_9\text{S}_8/\text{CNS}$  nanocomposite is proposed. Compared to pure  $\text{Co}_9\text{S}_8$ , the  $\text{Co}_9\text{S}_8/\text{CNS}$  catalyst exhibits better electrocatalytic activity, impressive durability, lower overpotential at a current density of  $10 \text{ mA cm}^{-2}$  and a smaller Tafel slope. Moreover, the performance of the as-prepared electrocatalyst is better than the benchmark  $\text{RuO}_2$  and any other cobalt-based chalcogenides reported to date. We, therefore, believe that the synthetic method developed in this work can be further extended to synthesise a wide variety of metal-sulfide and carbon nanocomposites for energy conversion and storage applications.

## Acknowledgements

This work was financially supported by Australian Research Council (ARC) Discovery Project and the National Natural Science Foundation of China (Grant No. 51372248, 51432009).

## Notes and references

- M. G. Walter, E. L. Warren, J. R. McKone, S. W. Boettcher, Q. Mi, E. A. Santori and N. S. Lewis, *Chem. Rev.*, 2010, **110**, 6446.
- J. Luo, J. H. Im, M. T. Mayer, M. Schreier, M. K. Nazeeruddin, N. G. Park, S. D. Tilley, H. J. Fan and M. Grätzel, *Science*, 2014, **345**, 1593.
- Y. Li, M. Gong, Y. Liang, J. Feng, J. E. Kim, H. Wang, G. Hong, B. Zhang and H. Dai, *Nat. Commun.*, 2013, **4**, 1805.
- H. Dau, C. Limberg, T. Reier, M. Risch, S. Roggan and P. Strasser, *ChemCatChem*, 2010, **2**, 724.
- Y. Matsumoto and E. Sato, *Mater. Chem. Phys.*, 1986, **14**, 397.
- M. Liao, G. Zeng, T. Luo, Z. Jin, Y. Wang, X. Kou and D. Xiao, *Electrochim. Acta*, 2016, **194**, 59.
- Y. R. Zheng, M. R. Gao, Q. Gao, H. H. Li, J. Xu, Z. Y. Wu and S. H. Yu, *Small*, 2015, **11**, 182.
- M. Gong, Y. Li, H. Wang, Y. Liang, J. Z. Wu, J. Zhou, J. Wang, T. Regier, F. Wei and H. Dai, *J. Am. Chem. Soc.*, 2013, **135**, 8452.
- S. Jung, C. C. L. McCrory, I. M. Ferrer, J. C. Peters and T. F. Jaramillo, *J. Mater. Chem. A*, 2016, **4**, 3068.
- M. Al-Mamun, X. Su, H. Zhang, H. Yin, P. Liu, H. Yang, D. Wang, Z. Tang, Y. Wang and H. Zhao, *Small*, 2016, **12**, 2866.
- J. Liang, Y. Z. Wang, C. C. Wang and S. Y. Lu, *J. Mater. Chem. A*, 2016, **4**, 9797.
- N. Li, W. Y. Xia, J. Wang, Z. L. Liu, Q. Y. Li, S. Z. Chen, C. W. Xu and X. H. Lu, *J. Mater. Chem. A*, 2015, **3**, 21308.
- T. Gao, Z. Jin, M. Liao, J. Xiao, H. Yuan and D. Xiao, *J. Mater. Chem. A*, 2015, **3**, 17763.
- Y. Li and C. Zhao, *Chem. Mater.*, 2016, **28**, 5659.
- C. Xia, Q. Jiang, C. Zhao, M. N. Hedhili and H. N. Alshareef, *Adv. Mater.*, 2016, **28**, 77.
- B. Dong, X. Zhao, G. Q. Han, X. Li, X. Shang, Y. R. Liu, W. H. Hu, Y. M. Chai, H. Zhao and C. G. Liu, *J. Mater. Chem. A*, 2016, **4**, 13499.
- M. Al-Mamun, Z. Zhu, H. Yin, X. Su, H. Zhang, P. Liu, H. Yang, D. Wang, Z. Tang, Y. Wang and H. Zhao, *Chem. Commun.*, 2016, **52**, 9450.
- X. Lu, W. L. Yim, B. H. R. Suryanto and C. Zhao, *J. Am. Chem. Soc.*, 2015, **137**, 2901.

19. T. Y. Ma, S. Dai, M. Jaroniec and S. Z. Qiao, *Angew. Chem. Int. Ed.*, 2014, **53**, 7281.
20. Y. Liu, L. Yu, C. N. Ong and J. Xie, *Nano Res.*, 2016, **9**, 1983.
21. Y. Liu, H. Liu, Z. Zhou, T. Wang, C. N. Ong and C. D. Vecitis, *Environ. Sci. Technol.*, 2015, **49**, 7974.
22. S. Peng, X. Han, L. Li, Z. Zhu, F. Cheng, M. Srinivansan, S. Adams and S. Ramakrishna, *Small*, 2016, **12**, 1359.
23. Z. Lyu, J. Zhang, L. Wang, K. Yuan, Y. Luan, P. Xiao and W. Chen, *RSC Adv.*, 2016, **6**, 31739.
24. C. N. R. Rao and K. P. R. Pisharody, *Prog. Solid State Chem.*, 1976, **10**, 207.
25. W. Gu, L. Hu, W. Hong, X. Jia, J. Li and E. Wang, *Chem. Sci.*, 2016, **7**, 4167.
26. S. H. Chang, M. D. Lu, Y. L. Tung and H. Y. Tuan, *ACS Nano*, 2013, **7**, 9443.
27. L. L. Feng, M. Fan, Y. Wu, Y. Liu, G. D. Li, H. Chen, W. Chen, D. Wang and X. Zou, *J. Mater. Chem. A*, 2016, **4**, 6860.
28. C. H. Lai, M. Y. Lu and L. J. Chen, *J. Mater. Chem.*, 2012, **22**, 19.
29. N. Kumar, N. Raman and A. Sundaresan, *Z. Anorg. Allg. Chem.*, 2014, **640**, 1069.
30. S. Dou, L. Tao, J. Huo, S. Wang and L. Dai, *Energy Environ. Sci.*, 2016, **9**, 1320.
31. H. Wang, Z. Li, G. Li, F. Peng and H. Yu, *Catal. Today*, 2015, **245**, 74.
32. Y. Liu, C. Xiao, M. Lyu, Y. Lin, W. Cai, P. Huang, W. Tong, Y. Zou and Y. Xie, *Angew. Chem. Int. Ed.*, 2015, **127**, 11383.
33. J. Yang, G. Zhu, Y. Liu, J. Xia, Z. Ji, X. Shen and S. Wu, *Adv. Funct. Mat.*, 2016, **26**, 4712.
34. P. Ganesan, M. Prabu, J. Sanetuntikul and S. Shanmugam, *ACS Catal.*, 2015, **5**, 3625.
35. H. R. Chauke, D. Nguyen Manh, P. E. Ngoepe, D. G. Pettifor and S. G. Fries, *Phys. Rev. B*, 2002, **66**, 155105.
36. B. K. Barman and K. K. Nanda, *Dalton Trans.*, 2016, **45**, 6352.
37. H. Zhu, J. Zhang, R. Yanzhang, M. Du, Q. Wang, G. Gao, J. Wu, G. Wu, M. Zhang, B. Liu, J. Yao and X. Zhang, *Adv. Mater.*, 2015, **27**, 4752.
38. X. Cao, X. Zheng, J. Tian, C. Jin, K. Ke and R. Yang, *Electrochim. Acta*, 2016, **191**, 776.
39. H. R. Wenk and A. Bulakh, *Minerals: Their Constitution and Origin*, Cambridge University Press, UK, 2004.
40. X. Meng, H. Sun, J. Zhu, H. Bi, Q. Han, X. Liu and X. Wang, *New J. Chem.*, 2016, **40**, 2843.
41. Z. Wang, L. Pan, H. Hu and S. Zhao, *CrystEngComm*, 2010, **12**, 1899.
42. Y. Yin, C. K. Erdonmez, A. Cabot, S. Hughes and A. P. Alivisatos, *Adv. Funct. Mat.*, 2006, **16**, 1389.
43. I. Bezverkhy, P. Afanasiev and M. Danot, *J. Phys. Chem. B*, 2004, **108**, 7709.
44. H. Cui, R. D. Pike, R. Kershaw, K. Dwight and A. Wold, *J. Solid State Chem.*, 1992, **101**, 115.
45. D. M. Pasquariello, R. Kershaw, J. D. Passaretti, K. Dwight and A. Wold, *Inorg. Chem.*, 1984, **23**, 872.
46. W. Maneeprakorn, M. A. Malik and P. O'Brien, *J. Mater. Chem.*, 2010, **20**, 2329.
47. Y. X. Zhou, H. B. Yao, Y. Wang, H. L. Liu, M. R. Gao, P. K. Shen and S. H. Yu, *Chem.-Eur. J.*, 2010, **16**, 12000.
48. E. Bi, H. Chen, X. Yang, W. Peng, M. Gratzel and L. Han, *Energy Environ. Sci.*, 2014, **7**, 2637.
49. H. Hu, L. Han, M. Yu, Z. Wang and X. W. Lou, *Energy Environ. Sci.*, 2016, **9**, 107.
50. L. L. Feng, G. D. Li, Y. Liu, Y. Wu, H. Chen, Y. Wang, Y. C. Zou, D. Wang and X. Zou, *ACS Appl. Mater. Interfaces*, 2015, **7**, 980.
51. J. Liu, C. Wu, D. Xiao, P. Kopold, L. Gu, P. A. van Aken, J. Maier and Y. Yu, *Small*, 2016, **12**, 2354.
52. B. Jang, M. Park, O. B. Chae, S. Park, Y. Kim, S. M. Oh, Y. Piao and T. Hyeon, *J. Am. Chem. Soc.*, 2012, **134**, 15010.
53. A. Ferrari and J. Robertson, *Phys. Rev. B*, 2000, **61**, 14095.
54. Z. Tan, P. Liu, H. Zhang, Y. Wang, M. Al-Mamun, H. G. Yang, D. Wang, Z. Tang and H. Zhao, *Chem. Commun.*, 2015, **51**, 5695.
55. T. V. Sathisha, B. E. K. Swamy, S. Reddy, B. N. Chandrashekar and B. Eswarappa, *J. Mol. Liq.*, 2012, **172**, 53.
56. X. Meng, J. Deng, J. Zhu, H. Bi, E. Kan and X. Wang, *Sci. Rep.*, 2016, **6**, 21717.
57. G. Zhou, L. C. Yin, D. W. Wang, L. Li, S. Pei, I. R. Gentle, F. Li and H. M. Cheng, *ACS Nano*, 2013, **7**, 5367.
58. H. Yang, C. Shan, F. Li, D. Han, Q. Zhang and L. Niu, *Chem. Commun.*, 2009, 3880.
59. Y. Li, H. Zhang, Y. Wang, P. Liu, H. Yang, X. Yao, D. Wang, Z. Tang and H. Zhao, *Energy Environ. Sci.*, 2014, **7**, 3720.
60. F. Song and X. Hu, *J. Am. Chem. Soc.*, 2014, **136**, 16481.
61. J. Nai, H. Yin, T. You, L. Zheng, J. Zhang, P. Wang, Z. Jin, Y. Tian, J. Liu, Z. Tang and L. Guo, *Adv. Energy Mater.*, 2015, **5**, 1401880.
62. T. Y. Ma, S. Dai, M. Jaroniec and S. Z. Qiao, *J. Am. Chem. Soc.*, 2014, **136**, 13925.